Special Collection

Light-Driven Multi-Charge Separation in a Push-Pull Ruthenium-Based Photosensitizer – Assessed by RASSCF and TDDFT Simulations

Stephan Kupfer,*[a] Maria Wächtler,[a, b, d] and Julien Guthmuller[c]

The performance of photosensitizers in the field of, for example, solar energy conversion, relies on their light-harvesting efficiency in the visible region, population of long-lived charge-separated intermediates, as well as their charge-accumulation capacity amongst other properties. In this computational study, we investigate the photophysical properties of a bis(bipyridyl)ruthenium(II)-based black dye (**Ru**) incorporating a chromophoric unit based on a thiazole donor-acceptor push-pull motif. The combination of two light-harvesting units, that is, the Ru(II)polypyridyl and the thiazole-based organic dye, yields close-lying metal-to-ligand charge transfer (MLCT) states, involving both ligand spheres as well as intra-ligand charge transfer (ILCT) states of the organic dye. Due to the combination of inorganic and organic chromophores the computational modelling of the photophysics of **Ru** is challenging. To this aim, time-dependent density functional theory and multiconfigurational methods are applied. The excited-state properties obtained for the states of interest are rationalized by electronic absorption and resonance Raman spectroscopies. The CAM-B3LYP functional was found to accurately describe the ground- and excited-state properties of **Ru**. Finally, excited-state relaxation pathways and the multi-charge-accumulation capacity were addressed. Despite the unidirectional nature of the $MLCT_{thia}$ and $ILCT_{thia}$ transitions, the thiazole unit is merely capable to store one redox equivalent.

Introduction

The direct conversion of the energy contained in solar radiation into electricity or high-energy compounds, so-called solar fuels, is one of the main aims of chemists and physicists today. One field of this broad research topic is to develop photocatalytic systems for splitting water into hydrogen and oxygen converting solar energy into chemical energy.[1–6] Key steps in this process are efficient light-harvesting, the generation of separated charges and charge transfer to reaction sites where the actual catalytic reaction occurs. Each of these steps needs to be optimized to design artificial photosynthetic systems with optimal performance. Efficient light-harvesting can be achieved by designing systems with an absorption range covering as much of the visible spectral range as possible. One approach to achieve such panchromatic absorption is to combine multiple chromophoric units in large (supra)molecular architectures.[7–11] Although a broad absorption range can easily be achieved via this strategy, the main challenge is that the different chromophoric units need to be capable to funnel excitation energy towards a defined acceptor unit and/or to lead to generation of separated charges which are transferred to a defined acceptor, independent of the chromophoric unit excited by the absorption event. Further, the reactions involved in solar fuel production are involving multiple electrons while absorption of one photon usually generates only a single electron/hole pair. This multi-electron nature of the targeted reactions presents a special challenge, which needs to be considered in design of artificial light-harvesting units.[12–16] In an ideal scenario for efficient and broad band conversion of solar energy, excitation of all chromophoric units combined needs to lead to transfer of charge to a defined acceptor unit which can take up several redox equivalents and either is the reaction center or possesses the capability to serve as storage unit for several charge carriers transferred to a potential catalyst in a follow up reaction step.[8,17–20]

In the present contribution, we evaluate the light-harvesting efficiency and multi-electron storage capacity of such a panchromatic absorbing black dye with (potential) application

[a] Dr. S. Kupfer, Dr. M. Wächtler
Institute of Physical Chemistry
Friedrich Schiller University Jena,
Helmholtzweg 4, 07743 Jena (Germany)
E-mail: stephan.kupfer@uni-jena.de
[b] Dr. M. Wächtler
Department Functional Interfaces
Leibniz Institute of Photonic Technology Jena (Leibniz-IPHT),
Albert-Einstein-Straße 9, 07745 Jena (Germany)
[c] Dr. J. Guthmuller
Institute of Physics and Computer Science
Faculty of Applied Physics and Mathematics
Gdańsk University of Technology,
Narutowicza 11/12, 80233 Gdańsk (Poland)
[d] Dr. M. Wächtler
Abbe Center of Photonics (ACP)
Albert-Einstein-Straße 6
07745 Jena, Germany

Supporting information for this article is available on the WWW under https://doi.org/10.1002/cptc.202200010

Special Collection An invited contribution to the "GDCh and ChemPhotoChem: 5-Year Anniversary" Special Collection

as photosensitizer in the scope of solar energy conversion, i.e., dye-sensitized solar cells and solar fuels. The synthesis as well as the (experimental) characterization of this photosensitizer (**Ru**, Figure 1), covering, for example, electrochemistry as well as electronic absorption and emission spectroscopy, was reported previously by the Beckert group.[21]

Ru incorporates a donor-acceptor ligand bridged by a 4-methoxy-thiazole – based on the natural occurring luciferin, the light-emitting dye of fireflies – as well as a complementary bipyridyl ligand sphere. Therefore, the present transition metal complex combines two light-harvesting units, namely the thiazole-based organic dye as well as the inorganic chromophore based on the photophysics of the Ru(II) center. In consequence, **Ru** features a rich photoredox chemistry governed by metal-to-ligand charge transfer (MLCT) processes involving the metal center and both ligand spheres ($MLCT_{bpy}$ and $MLCT_{thia}$) as well as intra-ligand charge transfer events of the thiazole-based chromophore ($ILCT_{thia}$), see Figure 1. Of particular interest are the close-lying $MLCT_{thia}$ and $ILCT_{thia}$ transitions in the visible region, both directed towards the accepting pyridyl moiety of the push-pull thiazole ligand, thus, pointing to a potential multi-photoelectron storage on this moiety. Very recently, structurally related Ru(II) complexes with thiazole π-extended dipyridophenazine (dppz) ligands were reported by the group of Mary Price. The joint synthetic-spectroscopic study – assisted by quantum chemical simulations performed at the time-dependent density functional (TDDFT) level of theory – allowed to identify such MLCT and ILCT branching dynamics upon visible-light excitation.[22] However, the multi-electron storage capacity of the dppz acceptor ligand was not investigated; noteworthy, electrochemical or light-driven accumulation of several redox equivalents on the dppz motif was found to be unfavorable for structurally related transition metal complexes.[23–27]

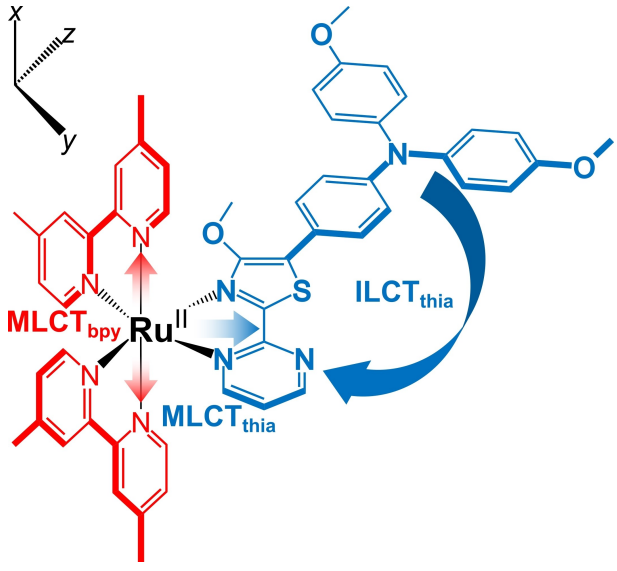

Figure 1. Structure of the investigated ruthenium(II) photosensitizer incorporating a thiazole-based conjugated donor-acceptor push-pull ligand, **Ru**.[21] Prominent electronic transitions, such as metal-to-ligand charge transfer from Ru to the bipyridyl ($MLCT_{bpy}$, in red) as well as to the $MLCT_{thia}$ (in blue) and intraligand charge transfer ($ILCT_{thia}$, in blue) towards the coordinated thiazole-pyrazyl moiety are indicated.

In addition to **Ru**'s potential application as photosensitizer with potential multi-electron storage capacity, the theoretical modelling of photophysical and photochemical properties of this class of transition metal complexes featuring a push-pull organic chromophore is exceptionally challenging. Structurally closely related ligands were already successfully studied by both TD(DFT)[21,28–33] as well as by MS-RASPT2//RASSCF.[29,33] These computational studies highlighted that ground state properties, i.e., the localization of single and double bonds, may affect the excited-state properties, such as excitation energies and transition dipole moments as well as excited-state gradients and equilibrium structures, significantly. As shown by Kupfer et al.,[29] range-separated (CAM-B3LYP) and global hybrids with a high ratio of exact exchange (M06-2X) allow an unbiased prediction of ground and excited-state properties. This finding was rationalized by multiconfigurational calculations, i.e., at the MS-RASPT2//RASSCF level of theory. However, hybrid functionals with lower amount of exact exchange are known to provide a reasonable compromise between computational cost and accuracy to assess the photophysics of transition metal complexes, i.e., for MLCT transition.[34–42] The difficulty for the present black dye is that both types of excitations (MLCT and ILCT) contribute significantly to its photophysics, which prevents a straightforward application of standard TDDFT methods, while multiconfigurational simulations are hampered by the size of the chemical systems.

Therefore, the present computational study aims to elucidate the photophysics, namely the interplay of the close-lying excited states of ILCT and MLCT nature, of **Ru** within the Franck-Condon region. To this end, the ground and excited-state properties of **Ru** are investigated by a series of (TD)DFT methods and compared to multiconfigurational results as well as to experimental data obtained by UV-vis absorption and resonance Raman spectroscopy. Finally, the excited-state relaxation channels and the multi-electron storage capacity of **Ru** are investigated.

Results and discussion

Franck-Condon photophysics and unidirectional light-harvesting

The first aim of the present contribution is to establish a computational protocol to assess the excited-state properties of the low-lying transitions in **Ru** – as given by the experimental absorption spectrum – in an unbiased fashion. The standard B3LYP[43,44] functional in combination with a double-ζ basis set has been shown to provide a good compromise between computational cost and accuracy for the MLCT excitations present in 4d and 5d transition metal complexes.[34–42] However, in the case of organic push-pull chromophores, long-range corrected XC functionals are known to provide a better description of their ILCT states.[28,29,45–49] The difficulty for the present ruthenium complex is that both types

of excitations (MLCT and ILCT) contribute significantly to its absorption spectrum as well as to its photochemistry. Therefore, the functionals B3LYP, B3LYP35[34,50] and CAM-B3LYP[51] were applied, both for the ground state geometry and for the excited-state properties, in order to identify a suitable method to reliably assess **Ru**'s photophysics (Figure 2 and Table 1).

The B3LYP XC functional strongly underestimates the energy of the intense ILCT state (S_1), but predicts an MLCT state (S_6) at 462–472 nm close to the first experimental band, see the energy histogram in Figure 3 for details. The MLCT state is assigned to the experimental shoulder at 435 nm, which leads to a typical deviation for TD-B3LYP of about −0.2 eV between the calculated and measured energies. However, the oscillator strength of the MLCT state (~0.08–0.09) appears underestimated in comparison to experiment. The B3LYP35 XC functional provides a good prediction of the ILCT state position, in particular when the CAM-B3LYP ground state geometry is employed (deviation of only −0.1 eV). The hypsochromic shift of the ILCT excitation going from the B3LYP geometry to the CAM-B3LYP geometry (+0.11 eV) is related to the increased localization of single and double bonds of the thiazole ligand.[29] Moreover, B3LYP35 presents a larger overestimation of the MLCT state (S_5) energy (deviation of 0.3 eV) than B3LYP, and similarly to B3LYP the oscillator strength is underestimated. The TD-CAM-B3LYP calculations shift the ILCT excitation (S_1) to higher energies, leading to a deviation of about 0.2–0.3 eV in

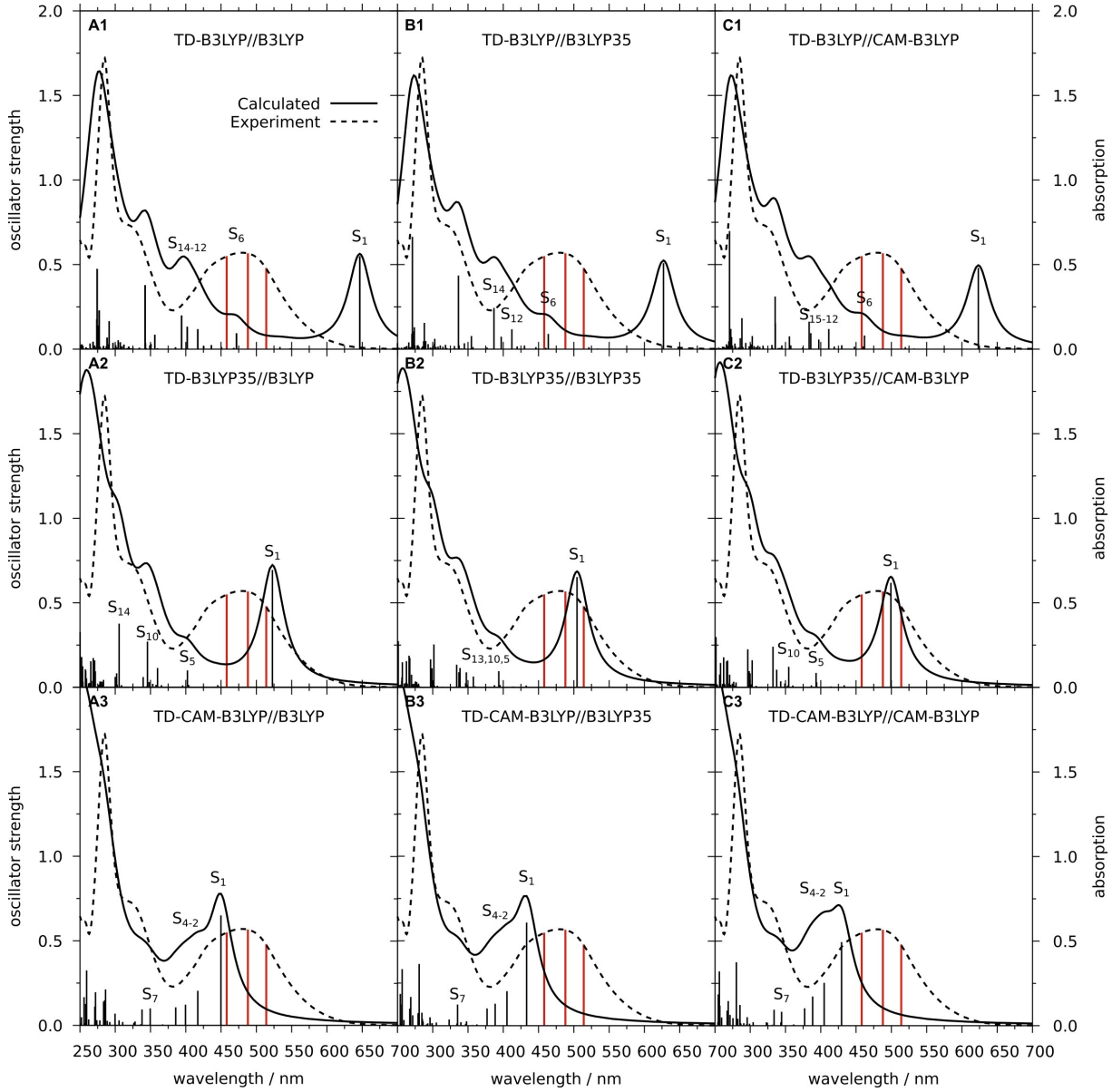

Figure 2. Simulated (solid black) and experimental (dashed) electronic absorption spectra of **Ru** in acetonitrile. Simulated spectra were obtained at the ESM//GSM (excited-state method//ground state method) level of theory, while the excited-state properties were determined within the fully optimized ground state structure as obtained by means of the B3LYP, B3LYP35 and CAM-B3LYP, respectively. Red vertical bars indicate excitation wavelengths (i.e., 514, 488 and 458 nm) used in resonance Raman experiments; black vertical bars show the positions and oscillator strengths of the electronic transitions. Prominent intra-ligand and metal-to-ligand charge transfer excitations are indicated.

Table 1. Vertical excitation energies (ΔE), wavelengths (λ), oscillator strengths (f) and singly excited configurations of the main singlet states calculated at the ESM//GSM as well as at the SA-RASSCF//CAM-B3LYP levels of theory, and experimental wavelengths (λ_{exp}).

GSM	ESM	Transition	weight [%]	state	ΔE [eV]	λ [nm]	f	λ_{exp} [nm]
B3LYP	B3LYP	$\pi_{thia,6}(235)\rightarrow\pi^*_{thia,1}(236)$ (ILCT)	98	S_1	1.92	647	0.5493	480
		$d_{xy}(232)\rightarrow\pi^*_{thia,1}(236)$ (MLCT)	84	S_6	2.63	472	0.0943	435
	B3LYP35	$\pi_{thia,6}(235)\rightarrow\pi^*_{thia,1}(236)$ (ILCT)	93	S_1	2.37	523	0.6939	480
		$d_{xy}(232)\rightarrow\pi^*_{thia,1}(236)$ (MLCT)	79	S_5	3.08	402	0.1003	435
	CAM-B3LYP	$\pi_{thia,6}(235)\rightarrow\pi^*_{thia,1}(236)$ (ILCT)	59	S_1	2.76	450	0.6496	480
		$d_{xz}(234)\rightarrow\pi^*_{thia,1}(236)$ (MLCT)	33					
		$d_{yz}(233)\rightarrow\pi^*_{thia,1}(236)$ (MLCT)	34	S_2	2.97	417	0.2046	435
		$d_{xz}(234)\rightarrow\pi^*_{thia,1}(236)$ (MLCT)	33					
		$\pi_{thia,6}(235)\rightarrow\pi^*_{thia,1}(236)$ (ILCT)	14					
B3LYP35	B3LYP	$\pi_{thia,6}(235)\rightarrow\pi^*_{thia,1}(236)$ (ILCT)	99	S_1	1.98	627	0.5088	480
		$d_{xy}(232)\rightarrow\pi^*_{thia,1}(236)$ (MLCT)	83	S_6	2.67	464	0.0900	435
	B3LYP35	$\pi_{thia,6}(235)\rightarrow\pi^*_{thia,1}(236)$ (ILCT)	93	S_1	2.46	505	0.6525	480
		$d_{xy}(232)\rightarrow\pi^*_{thia,1}(236)$ (MLCT)	78	S_5	3.15	394	0.0958	435
	CAM-B3LYP	$\pi_{thia,6}(235)\rightarrow\pi^*_{thia,1}(236)$ (ILCT)	57	S_1	2.86	433	0.6097	480
		$d_{xz}(234)\rightarrow\pi^*_{thia,1}(236)$ (MLCT)	34					
		$d_{xz}(234)\rightarrow\pi^*_{thia,1}(236)$ (MLCT)	36	S_2	3.06	405	0.2036	435
		$d_{yz}(233)\rightarrow\pi^*_{thia,1}(236)$ (MLCT)	32					
		$\pi_{thia,6}(235)\rightarrow\pi^*_{thia,1}(236)$ (ILCT)	15					
CAM-B3LYP	B3LYP	$\pi_{thia,6}(235)\rightarrow\pi^*_{thia,1}(236)$ (ILCT)	99	S_1	1.99	623	0.4801	480
		$d_{xy}(232)\rightarrow\pi^*_{thia,1}(236)$ (MLCT)	74	S_6	2.68	462	0.0806	435
	B3LYP35	$\pi_{thia,6}(235)\rightarrow\pi^*_{thia,1}(236)$ (ILCT)	93	S_1	2.48	499	0.6185	480
		$d_{xy}(232)\rightarrow\pi^*_{thia,1}(236)$ (MLCT)	72	S_5	3.15	393	0.0856	435
		$\pi_{thia,6}(235)\rightarrow\pi^*_{bpy,1}(237)$ (LLCT)	14					
	CAM-B3LYP	$\pi_{thia,6}(235)\rightarrow\pi^*_{thia,1}(236)$ (ILCT)	48	S_1	2.89	429	0.4943	480
		$d_{xz}(234)\rightarrow\pi^*_{thia,1}(236)$ (MLCT)	42					
		$d_{yz}(233)\rightarrow\pi^*_{thia,1}(236)$ (MLCT)	33	S_2	3.06	405	0.2537	435
		$d_{xz}(234)\rightarrow\pi^*_{thia,1}(236)$ (MLCT)	31					
		$\pi_{thia,6}(235)\rightarrow\pi^*_{thia,1}(236)$ (ILCT)	20					
	SA-RASSCF	$d_{xy}\rightarrow\pi^*_{thia,1}$ (MLCT)	79	Root 4	3.60	361	0.1561	435
		$\pi_{thia,6}\rightarrow\pi^*_{thia,1}$ (ILCT)	78	Root 5	4.10	302	0.7898	480
		$d_{xz}\rightarrow\pi^*_{bpy,1}$ (MLCT)	74	Root 7	4.24	292	0.1605	435

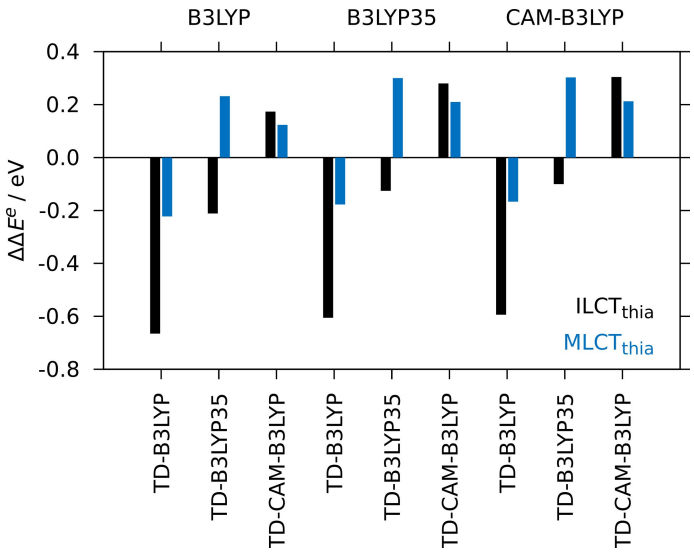

Figure 3. Energy histogram for prominent low-lying dipole-allowed $ILCT_{thia}$ (black) and $MLCT_{thia}$ (blue) transitions, see Table 1, as obtained at the ESM//GSM (excited-state method//ground state method) level of theory. Energy deviations are given with respect to features of the experimental UV-vis absorption spectrum at 2.58 and 2.85 eV for $ILCT_{thia}$ and $MLCT_{thia}$, respectively.

comparison to experiment. It is also noticed that the ILCT and MLCT transitions are significantly mixed. The stronger mixing occurs with the CAM-B3LYP geometry, for which a transfer of intensity from the ILCT state (S_1) toward the MLCT state (S_2) is obtained. Additionally, the energy of the MLCT state is lower in comparison to B3LYP35, which improves the agreement with experiment, i.e., deviation of +0.21 eV at the TD-CAM-B3LYP//CAM-B3LYP level. Therefore, apart from a systematic overestimation of the ILCT and MLCT excitation energies (about 0.2–0.3 eV), the absorption spectrum obtained with the TD-CAM-B3LYP//CAM-B3LYP method presents the best agreement with the experimental spectrum: *i)* the energy gap between the

ILCT and MLCT excitations is better reproduced by TD-CAM-B3LYP calculations, and *ii)* the relative intensities of the ILCT and MLCT states are more accurate using the TD-CAM-B3LYP//CAM-B3LYP level of theory. Furthermore, it can be mentioned that a previous study[29] on a comparable thiazole dye has shown that the CAM-B3LYP XC functional is better suited for the ground state geometry. Additionally, MLCT states (S_3 and S_4) with noticeable oscillator strengths are obtained close in energy to the MLCT excitation (S_2). These states also provide a contribution to the first absorption band in the TD-CAM-B3LYP calculations. Details with respect to the electronic transitions as well as regarding the involved molecular orbitals are summarized in the supporting information (Tables S1–S7).

Calculations of the fractional occupation density (FOD) were performed in order to estimate the importance of static electron correlation within the singlet ground state. The FODs (Figure S2) as obtained within the B3LYP, B3LYP35 and CAM-B3LYP equilibrium structures show that nearly all non-hydrogen atoms present contributions to the electronic correlation.

The larger contributions are given by the ruthenium atom, the nitrogen atoms coordinated to the ruthenium, as well as several of the carbon, nitrogen and oxygen atoms of the thiazole-based ligand. This result indicates that multi-configurational methods are required to describe the electronic structure of the transition metal complex at hand within the singlet ground state, however, and in particular regarding the MLCT and ILCT excitations. Therefore, SA-RASSCF calculations were performed to investigate this aspect and to provide a comparison with the TDDFT results.

As described in the computational methods section, two different active spaces and two different partitions of the orbitals were considered to describe the $MLCT_{bpy}$, $MLCT_{thia}$ and $ILCT_{thia}$ excitations. The results obtained using the CAM-B3LYP geometry are given in-depth within the supporting information (Tables S8 and S9), while the main MLCT and ILCT excitations calculated with the second partition of the orbitals are reported in Table 1. In all cases, the electronic ground state (root 1) is quantitatively described by the Hartree-Fock reference wavefunction with a weight between 82 and 90%. The SA-RASSCF calculations on the higher roots predict a dipole-allowed $MLCT_{bpy}$ transition at 4.24 eV with an oscillator strength of 0.16 (Table 1). The energy of this state is unaffected by the orbital partitioning of RAS_{bpy} (Table S9), i.e. (18,2,2;4,9,2) vs. (18,2,2;6,5,4). Additionally, the multi-configurational calculations yield an intense $ILCT_{thia}$ excitation at 4.10 eV ($f=0.79$) and a weaker $MLCT_{thia}$ state at 3.60 eV ($f=0.16$) having the same orbital characters as those obtained at TDDFT level of theory. However, the energies of these states are more sensitive to the employed orbital partition (Table S8). Interestingly, and independent of the orbital distribution within the RAS subspaces, the $ILCT_{thia}$, $MLCT_{thia}$ and $MLCT_{bpy}$ states feature a more pronounced multiconfigurational character as the electronic ground state (Tables S8 and S9). This highly mixed character is exclusively predicted by TD-CAM-B3LYP – independent of the provided GSM. TD-B3LYP and TD-B3LYP35 yield weights of roughly 80–100% for the respective leading transitions of these $ILCT_{thia}$, $MLCT_{thia}$ and $MLCT_{bpy}$ excitations. It is also observed that the SA-RASSCF method predicts the positions of the $ILCT_{thia}$ and $MLCT_{thia}$ states with the opposite order to TDDFT and experiment, and their energies are significantly overestimated by 1.52 eV and 0.75 eV in comparison to the experimental results, respectively. This deviation is not surprising and can be ascribed to the lack of dynamical electron correlation, which can in principle be included by RASPT2. Unfortunately, (MS-)RASPT2 calculations could not be performed for the present transition metal complex due to their enormous computational demand.

RR spectra were simulated and compared to experimental data (Figure 4) in order to further evaluate the computational

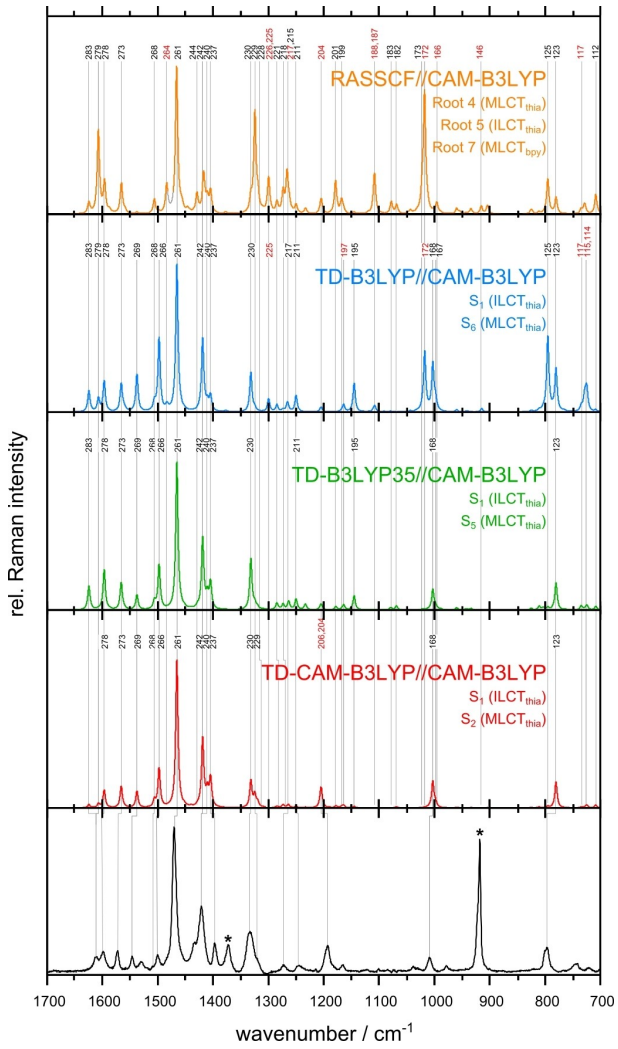

Figure 4. Experimental (in black) and simulated resonance Raman spectra as obtained using the sum-over states formalism upon 514 nm excitation. Excited-state contributions (transition dipole moments and excited-state gradients) were considered by SA-RASSCF (excited-state method, ESM) for three prominent $ILCT_{thia}$, $MLCT_{thia}$ and $MLCT_{bpy}$ transitions (see SA(10)-RASSCF (18,2,2;4,9,2) and SA(10)-RASSCF (18,2,2;6,5,4) in Figure S2 and Table S8 and S9). At the TD-B3LYP, TD-B3LYP35 and TD-CAM-B3LYP levels of theory (ESM) only $ILCT_{thia}$ and $MLCT_{thia}$ states were considered. All calculations were performed within the CAM-B3LYP ground state equilibrium (ground state method, GSM). Prominent vibrational normal modes centered at the thiazole (in black) as well as at the bipyridyl ligands (in red) are labeled and assigned to experimental data; solvent bands in the experimental data set are indicated by asterisk.

methods. The RR intensities were obtained for an excitation wavelength of 514 nm using the CAM-B3LYP geometry for the ground state and B3LYP, B3LYP35, CAM-B3LYP and RASSCF for the excited-state properties (i.e., transition dipole moments and excited-state gradients). The spectra for the other excitation wavelengths (488 nm and 458 nm), the other ground state geometries as well as the individual contributions of the excited states estimated with the short-time approximation (STA) (i.e., gradient approximation) are reported in the supporting information (Figures S3–S10). In the simulations, the excitation energies of the ILCT and MLCT states were set at the experimental values (2.58 and 2.85 eV, respectively) to allow a comparison among the methods.

The comparison between the RR spectra obtained with different ground state geometries (Figure S6–S8 for 514, 488 and 458 nm excitation) shows that the CAM-B3LYP geometry provides the best agreement with the experimental RR data. In Figure 4, it is apparent that the B3LYP//CAM-B3LYP method overestimates the RR intensities below 1100 cm^{-1}. However, the B3LYP35 and CAM-B3LYP functionals improve the B3LYP result and consequently provide a superior agreement with the experimental reference spectrum. Furthermore, the STA RR spectra (Figures S3–S5) show that both $ILCT_{thia}$ and $MLCT_{thia}$ states enhance the vibrational modes localized on the thiazole-based ligand. Nevertheless, a noticeable difference concerns triphenyl amin centered mode 283 at 1624 cm^{-1} (Table S12), which is only present in the STA RR spectrum of $ILCT_{thia}$ (S_1) as this group acts as donor in $ILCT_{thia}$, yet it is not involved in the respective $MLCT_{thia}$ transition. The presence of this band in the experimental RR spectrum recorded at 514 nm and its decreased intensity for shorter excitation wavelengths (Figure S9), i.e., for 488 and 458-nm excitation, indicates that the $ILCT_{thia}$ state is localized below the $MLCT_{thia}$ state – in agreement with all performed TDDFT simulations.

The calculation performed with the RASSCF//CAM-B3LYP method shows some general agreement with the experimental RR spectrum but are less accurate than the TDDFT RR spectra due to some inconsistencies in the relative RR intensities. This indicates that the inclusion of dynamical electron correlation effects is also mandatory for the simulation of RR spectra and for the calculation of excited-state gradients in case of the present transition metal complex, which is in contrast to previous computational studies on organic chromophores.[29,52] Overall, the analysis of the RR spectra confirms the choice of the TD-CAM-B3LYP//CAM-B3LYP method to investigate the excited-state properties and the multi-electron storage capacity, which is considered in the following section. Noteworthy, non-Condon effects (i.e. Herzberg-Teller effects), which can be described by calculating the transition polarizability tensor along the distortion of the vibrational normal modes,[53–55] seem to be of minor importance in case of the present transition metal complex, as evident from the comparison of the RR intensity pattern obtained by TD-CAM-B3LYP//CAM-B3LYP and the experimental reference spectrum (Figure 4).

Excited-state relaxation and site-specific multi-electron storage capacity

Upon careful elucidation of the excited states involved in the initial photoexcitation within the visible region as well as studying prominent excited-state relaxation channels in the Franck-Condon point – depending on the computational description of the electron ground state as well as of the excited states – the potential of **Ru** to collect two electrons on a specific ligand sphere is investigated. In case of the present photosensitizer, multi-electron storage on the thiazole ligand is addressed. Such storage capacity is of utmost importance in the scope of solar-driven hydrogen production using supramolecular photocatalysts composed of *i*) a photosensitizer, *ii*) a catalytic active site as well as *iii*) a central bridging ligand architecture which functions as electron relay and allows the electronic communication between *i)* and *ii)*. Therefore, the capacity of the electron relay to store several photoexcited electrons is highly desirable in the scope of photocatalytic hydrogen productions – as two electrons are needed to form molecular hydrogen from a proton source. In the following, we investigate the multi-electron storage capacity of the thiazole ligand in **Ru** based on a second photoexcitation of the charge-separated intermediate as well as by simulation of sequential electrochemical reduction events.

In order to evaluate such second light-driven charge-separation process, we need to study the excited-state relaxation of the initial photoexcitation in more detail; here we focus exclusively on the TD-CAM-B3LYP//CAM-B3LYP data which was shown in the previous section to provide a reliable picture of structural and excited-state properties. Figure 5A shows the simulated absorption spectrum obtained at the TD-CAM-B3LYP//CAM-B3LYP level of theory. The energy levels of low-lying strongly dipole-allowed singlet-singlet excitations within the Franck-Condon point (S_0 equilibrium structure) are visualized in Figure 5B.

In addition, prominent triplet states, involved in the subsequent, competitive excited-state relaxations channels are shown. Typically, ultrafast population transfer from the singlet to the triplet manifold is observed for structurally related transition metal complexes, i.e., upon ^{1}MLCT excitation.[56–58] In the present system, excitation into S_1 as well as into S_2 is expected to allow such population transfer to the adjacent triplet state via intersystem crossing (ISC) as a result of the pronounced mix of both $^1ILCT_{thia}$ and $^1MLCT_{thia}$ transitions. Of particular interest are the T_6 as well as the triplet ground state (T_1). On the first hand, the latter T_1, is of $^3ILCT_{thia}$ character as illustrated in Figure 5D, while the mixing of $ILCT_{thia}$ and $MLCT_{thia}$ contributions as observed for S_1 (and S_2) is abrogated upon ISC and equilibration. This $^3ILCT_{thia}$ state represents a potentially long-lived charge-separated triplet state, as charge recombination – either via phosphorescence or radiationless decay – is commonly hampered due to small spin-orbit couplings involving ^{3}ILCT states.[34,42,59] This triplet state is predicted at the TDDFT level of theory 1.41 eV above the singlet ground state, while a singlet-triplet gap of merely 1.21 eV is obtained at the DFT level of theory. Experimentally, two main emission bands

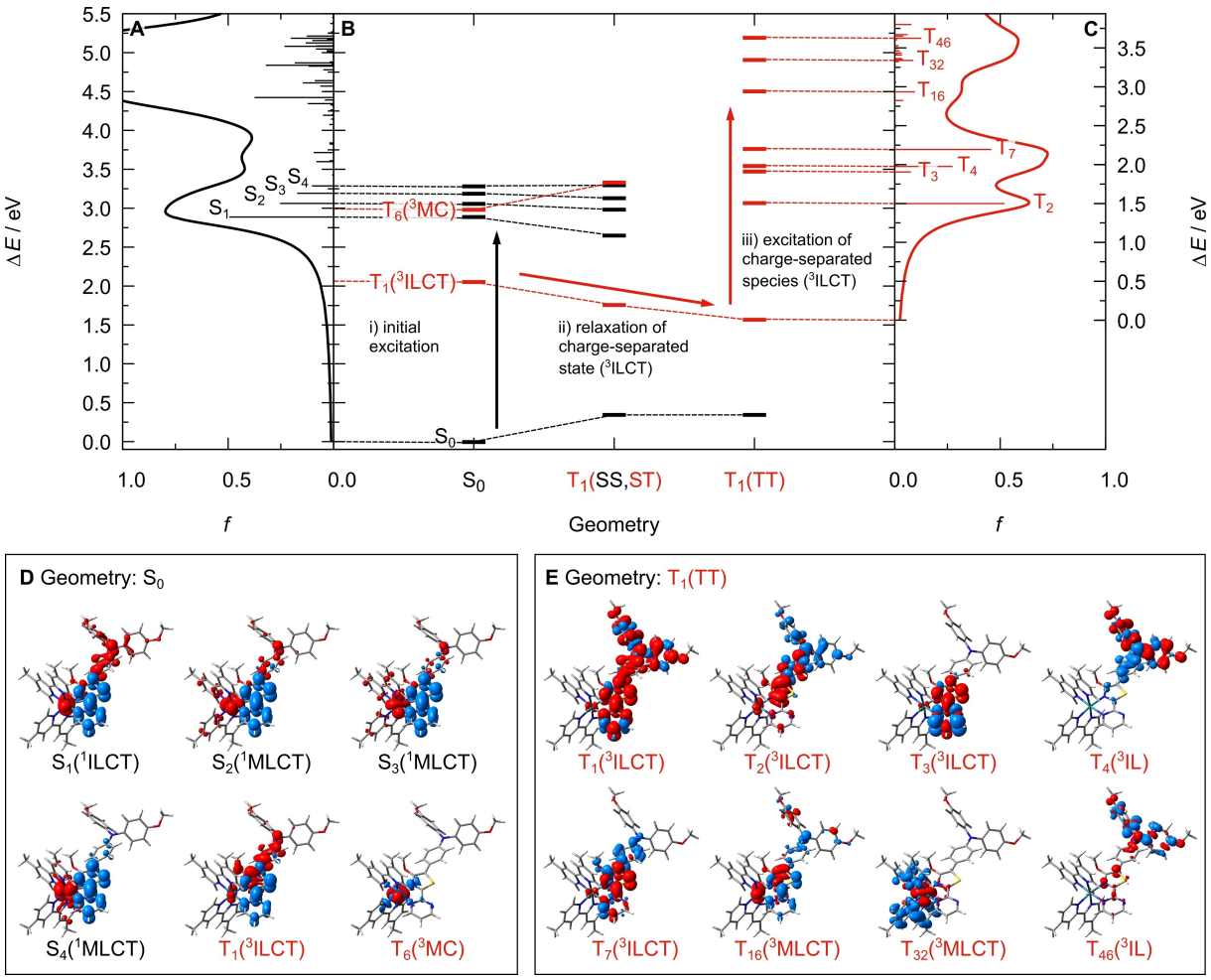

Figure 5. A: UV-vis absorption spectrum of **Ru** obtained at the TD-CAM-B3YLP//CAM-B3LYP level of theory. **B**: Singlet (in black) and triplet states (in red) involved in the subsequent excited-state relaxation from the Franck-Condon point (S_0 geometry) leading to the population of the $^3ILCT_{thia}$ ground state (T_1 geometry), see singlet-singlet and singlet-triplet transitions, i.e., T_1(SS, ST). Spin and dipole-allowed triplet-triplet transitions, i.e., T_1(TT), contributing to the excited-state absorption within the ^{3}ILCT equilibrium, **C**, are indicated. **D** and **E**: Electronic character of singlet-singlet and triplet-triplet transitions as illustrated by charge density differences within the S_0 and the T_1(TT) ground states, respectively. The nature of the triplet ground state, i.e., $T_1(^3ILCT_{thia})$, is visualized by the spin density.

at 1.97 and 1.68 eV (627 and 736 nm) were observed for **Ru** upon 400-nm excitation.[21] The emission feature at 1.68 eV can be associated to the predicted $^3ILCT_{thia}$ channel (TDDFT: 1.41 eV), while the second emission process presumably occurs via a $^3MLCT_{bpy}$ state.[60,61] On the other hand, the T_6 state, a so-called metal-centered (^{3}MC) state (Figure 5D), is predicted by TDDFT. Such ^{3}MC states are well-known to be involved in prominent excited-state relaxation pathways leading to charge recombination for related transition metal complexes.[60,62–65] Of particular interest is the low-excitation energy of this ^{3}MC state (2.98 eV, 416 nm) in the Franck-Condon point of **Ru**; typically such states associated to undesirable charge recombination processes are observed for ruthenium(II)-bipyridyl-based systems in the UV region.[66]

In the following, we focus on the excited-state relaxation channel leading to the population of the $^3ILCT_{thia}$ triplet ground state and a possibility of a subsequent second light-driven charge transfer event, for example, via a $^3MLCT_{thia}$ excitation, in more detail. Upon equilibration, the ^{3}ILCT state is substantially lowered from 2.05 to 1.56 eV while the order of the low-lying singlet states (S_1–S_4) is unaffected. This stabilization mainly originates from alterations of bond lengths involved in the aromatic structure of the thiazole ligand as well as from the partial planarization of the phenyl-thiazole moiety (S_0: 30.6°; T_1: 16.0°) as studied previously in-depth.[28,29,33] Simultaneously, the undesirable ^{3}MC state is destabilized by ~0.35 eV (to 3.33 eV). The electronic absorption spectrum of the $^3ILCT_{thia}$ state in its equilibrium is shown in Figure 5C, while prominent transitions are visualized by charge density differences (CDD) in Figure 5E. The low-lying excited triplet states, contributing to the dipole and spin-allowed triplet-triplet absorption, are exclusively localized on the thiazole ligand sphere, i.e., T_2, T_3, T_4 and T_7. In the frame of a potential second light-driven charge transfer onto the target ligand, dipole-allowed excitation in $^3ILCT_{thia}$ states T_3 and T_7 at 1.90 and 2.20 eV (653 and 564 nm), respectively, as well as into the $^3MLCT_{thia}$ state T_{16} at 2.94 eV (422 nm), see Figure 5E, are of potential interest. However, the oscillator strength of the $T_1 \rightarrow T_{16}$ excitation ($f = 0.0958$) is

significantly lower than the $S_0 \rightarrow S_1$ excitation ($f = 0.4943$, Table 1). In a similar fashion, the energetic position of the higher lying $^3MLCT_{bpy}$ state, T_{32} at 3.34 eV (371 nm, $f = 0.0887$), is hardly affected upon relaxation into the ^{3}ILCT ground state equilibrium structure, however its oscillator strength is considerably increased with respect to the S_5 state in the Franck-Condon region (3.42 eV, 362 nm, $f = 0.0074$). Additionally, one prominent low-lying ^{3}ILCT state, T_2 at 1.50 eV (827 nm, $f = 0.5214$), is predicted at the TD-CAM-B3LYP//CAM-B3LYP level of theory. Population of this ^{3}ILCT state is associated to charge transfer from the photoreduced thiazole-pyrimidyl acceptor moiety back to the triphenyl amino donor, thus, leading to an undesired charge recombination process. In terms of a potential application of the present ruthenium-based black absorber as photosensitizer for light-harvesting and multi-electron storage, population of such charge recombination channel needs to be avoided, which could be easily rationalized by applying a filter to allow exclusively an excitation below ~600 nm. This way, a direct light-driven depopulation of the charge-separated ^{3}ILCT state is hampered and a subsequent second charge separation, leading a doubly photoreduced thiazole ligand, such as via the $^3MLCT_{thia}$ state (T_{16}) or the two $^3ILCT_{thia}$ states (T_3 and T_7), could be possible.

Finally, the multi-electron storage capacity of the thiazole ligand incorporated in **Ru** is assessed by stepwise electrochemical reduction events. Therefore, DFT simulations at the CAM-B3LYP level of theory are performed for the singly and doubly reduced species of **Ru**. In case of the first reduction step, the accessory charge can be either localized on the bipyridyl or the thiazole-based ligand sphere. Both singly reduced species, i.e., ^{2}**Ru1**$_{bpy}$ as well as ^{2}**Ru1**$_{thia}$, were fully optimized, see spin densities in Figure 6A and B.

In accordance with the excited-state properties of the low-lying singlet transitions in **Ru**, a thiazole-based first reduction (^{2}**Ru1**$_{thia}$) was calculated to be favored by approximately 0.55 eV with respect to a bpy-centered reduction (^{2}**Ru1**$_{bpy}$). Subsequently, the doubly reduced complex was fully optimized from the ^{2}**Ru1**$_{thia}$ equilibrium structure, while two redox states were considered, namely the doubly reduced singlet (^{1}**Ru2**) as well as the doubly reduced triplet species (^{3}**Ru2**). The former ^{1}**Ru2** features both additional electrons in the lowest π_{thia}* orbital as shown in Figure 6C. Thus, in case of the singlet species, both reduction events take place on the thiazole ligand – demonstrating its ability to store several electrons. However, the triplet version of the doubly reduced complex localizes the second reduction event on one of the two bpy ligands, as illustrated by the spin density of ^{3}**Ru2** in Figure 6D. Thermodynamically, the formation of ^{3}**Ru2** is more favorable by ~0.25 eV with respect to ^{1}**Ru2**. Therefore, the second electrochemically introduced electron is likely not stored on the thiazole-sphere. Electrochemical experiments show three reversible reduction events at approx. −1.4, −2.0, and −2.2 V,[21] which are likely associated to the reduction of the thiazole ligand (first reduction) as well as to the stepwise reduction of each bpy ligand (second and third reduction) – given the insight obtained by the present quantum chemical investigation. However, structural modification of the bpy-ligands, such as with electron donating groups, might tunes the relative electron acceptor potentials in **Ru** sufficiently to allow a stepwise double reduction on the target ligand. Alternatively, the electron deficient bipyridyl ligand can be replaced by electron rich ligands, such as, for example, carbene or biimidazole ligands, in order to localize the excited-state relaxation and redox processes on the desired ligand sphere as shown very recently in the literature.[67–71]

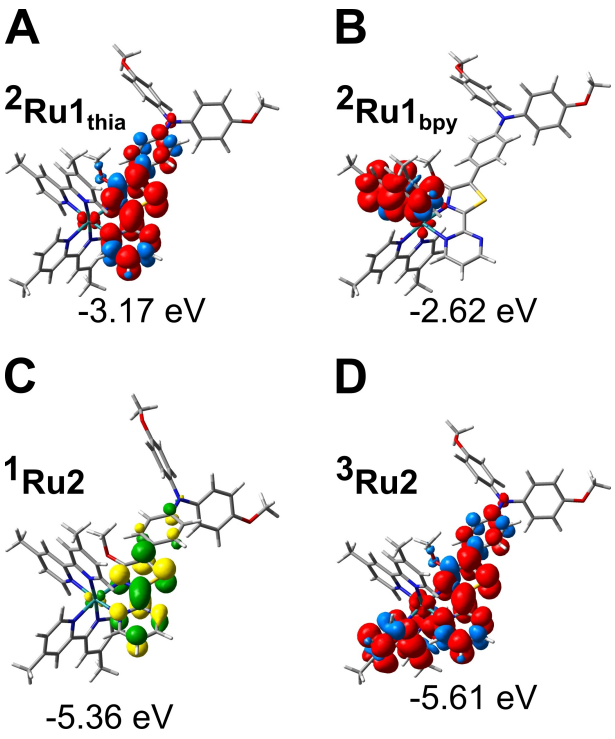

Figure 6. A and **B**, singly reduced doublet species of **Ru**, thiazole-based (^{2}**Ru1**$_{thia}$) and bipyridine-based (^{2}**Ru1**$_{bpy}$) reduction is considered. **C** and **D**, doubly reduced singlet and triplet species; **1Ru21**$_{thia}$ and **3Ru2**. Excess charge localization is visualized for open-shell systems (**A**, **B** and **D**) by the spin density and for closed-shell species (**C**) by the highest-occupied molecular orbital.

Conclusion

The present computational study carefully evaluates the excited states involved in the light-driven charge separation processes – as well as in a potential multi-charge separation – of a Ru(II)-polypyridyl-based black absorber (**Ru**), incorporating an auxiliary organic chromophore unit based on a push-pull ligand architecture. The excited-state landscape at the Franck-Condon point was assessed with TDDFT, using the hybrid functionals B3LYP and B3LYP35 and the range-separated CAM-B3LYP functional, while an additional impact of the electronic ground state method (B3LYP, B3LYP35 and CAM-B3LYP) was evaluated. The electronic structure of **Ru** is particularly challenging for TDDFT methods as both electronic transitions of MLCT and ILCT characters contribute to its electronic absorption within the visible region. The present study reveals that the equilibrium structure and the low-lying excited singlet

states of **Ru** are best described using the CAM-B3LYP functional, which was further supported by multi-configurational investigations as well as based on the comparison between experimental and simulated resonance Raman spectra at three excitation wavelengths covering **Ru**'s absorption band in the visible region.

The potential multi-photoelectron storage capacity of the thiazole ligand was investigated exclusively at the CAM-B3LYP level of theory. The excitation spectrum of the charge-separated triplet species of $^3ILCT_{thia}$ nature (triplet ground state) reveals several favorable ^3MLCT and ^3ILCT excitations that are capable of transferring a second electron on the singly photo-reduced thiazole-based ligand. However, $MLCT_{bpy}$ and low-lying metal-centered states were identified as competitive excited-state relaxation channels that hamper the population of such multi-charge-separated species. In agreement with electrochemical data, DFT simulations point to a stepwise reduction of first the thiazole ligand, followed by two reduction events localized on the bipyridyl ligands.

Future joint synthetic-spectroscopic-theoretical studies will aim to modify the electronic structure of related transition-metal-based photosensitizers, incorporating organic push-pull chromophores, by introducing unidirectional excited relaxation pathways based on photo-innocent ligand architectures. This concept is expected to allow localizing several (photo)reduction events on a desired target ligand sphere.

Computational methods

All ground state calculations, for **Ru** and its derivatives, were performed using Gaussian 09.[72] Density functional theory (DFT) was applied using the exchange-correlation (XC) functionals B3LYP[43,44] and B3LYP35,[34,50] which is a modified version of B3LYP including 35% of Hartree-Fock exchange, as well as the range-separated functional CAM-B3LYP.[51] The 6–31G(d)[73] double-ζ basis set was utilized for all main group elements and the MWB28[74] relativistic core potential with its double-ζ basis set was employed for ruthenium. Vibrational mode analysis verified that all ground state geometries are local minima on their respective potential energy surface (PES). To correct for the lack of anharmonicity and the approximate treatment of electron correlation, the harmonic frequencies were scaled by the factor 0.97 for B3LYP and by the factor 0.95 for B3LYP35 and CAM-B3LYP.[75,76]

Excited-state calculations were performed at the TDDFT level of theory using the same density functionals and basis sets as for the ground state calculations. The 100 lowest singlet excited states were calculated with the three considered functionals for each ground state geometries obtained with B3LYP, B3LYP35 and CAM-B3LYP, leading in consequence to a set of nine combinations denoted ESM//GSM, where ESM and GSM indicate the applied excited state (ESM) and ground state methods (GSM), respectively. Additionally, the (multiple) photoelectron storage capacity of the thiazole ligand of **Ru** was evaluated. Therefore, the non-reduced triplet species (^{3}**Ru**), two singly-reduced doublet species with the excess charge localized on the thiazole (^{2}**Ru1**$_{thia}$) vs. on the bipyridyl (^{2}**Ru1**$_{bpy}$) ligand sphere, the doubly-reduced singlet (^{1}**Ru2**) as well as the doubly-reduced triplet (^{3}**Ru2**) were investigated. For these redox-species, CAM-B3LYP was utilized exclusively as this functional proved to provide a balanced description of structural and electronic properties, as shown for **Ru**. The excited-state properties of ^{3}**Ru** were investigated at the TDDFT level of theory by means of the 100 lowest dipole-allowed triplet-triplet excitations. Application of the Tamm-Dancoff approximation (TDA), which often provides an improved energetic description of the low-lying triplet states,[77,78] was not considered as the main focus of the present study was to address the Franck-Condon photophysics of **Ru**. This is further justified as the energy of the triplet ground state in ^{3}**Ru**, i.e. of ^3ILCT character, differs merely by 0.2 eV as obtained by DFT (1.76 eV) vs. TDDFT (1.56 eV), see Figure 5B. To account for solvent effects (acetonitrile, $\varepsilon = 35.688$, $n = 1.344$), the integral equation formalism of the polarizable continuum model (IEF-PCM) was applied for all ground and excited-state properties, if not stated overwise.[79] In case of geometry optimizations, the equilibrium procedure of solvation was applied, while the non-equilibrium procedure of solvation was used for the calculation of excitation energies and excited-state gradient, which is well adapted for processes where only the fast reorganization of the electronic distribution of the solvent is important.

The fractional occupation density (FOD), as introduced by the Grimme group,[80,81] was calculated in order to assess and to visualize the impact of static electron correlation within the singlet ground state of the ruthenium metal complex (**Ru**). FODs for the B3LYP, B3LYP35 and CAM-B3LYP equilibrium structures were calculated by ORCA 4.1.0[82] using the meta-GGA functional TPSS[83] in conjunction with the def2-SV(P)[84,85] basis set, while a smearing temperature of 5000 K and the 'TightSCF' keyword were applied.

In order to describe static correlation – as visualized by the FODs – multiconfigurational methods, for example, the complete active space self-consistent field (CASSCF) approach,[86] are the methods of choice. Such multiconfigurational calculations allow to provide an unbiased description of the photophysics of small to medium sized chemical systems, for example, the light-driven charge accumulation capacity in **Ru**. Yet, the computational demand raises quickly with the size of the active space (AS). In case of the present transition metal complex, an appropriate AS would include a Ru-centered AS comprising ten electrons in seven molecular orbitals, (10,7), a (12,12) with the π_{bpy}/π^*_{bpy} system of each bipyridine (bpy) ligand, as well as a (20,18) containing the π_{thia}/π^*_{thia} orbitals of the thiazol-based ligand. Consequentially, an AS (54,49) is obtained for **Ru** – leading to more than 10^{26} configuration state functions (CSFs), which is unfeasible without further restrictions. To contain the number of CSFs in the CASSCF methodology, several approaches have been introduced, for example, the general active space (GAS)SCF[87–89] and split-GAS,[90] the occupation-restricted multiple-active-space (ORMAS)[91] model, the density matrix renormalization group (DMRG)[92–95] or the restricted active space (RAS)SCF[96–98] method. In case of the latter RASSCF approach, the AS is fragmented into three subspaces: one which holds mostly doubly occupied orbitals with a predefined number of maximal electron holes (RAS1), the RAS2 subspace where a full configuration interaction calculation is performed, and a subspace with mostly unoccupied orbitals (RAS3) where a defined number of electrons is allowed to be excited into. In order to label the RAS calculations, the notation RAS (*n*,*l*,*m*;*i*,*j*,*k*) of Gagliardi and co-workers[99] is used. The index *n* labels the number of active electrons, *l* is the maximum number of holes in the RAS1, and *m* is the maximum number of electrons in the RAS3. The labels *i*, *j*, and *k* refer to the number of active orbitals in RAS1, RAS2, and RAS3, respectively. All multiconfigurational calculations were performed as implemented in MOLCAS 8.0 using the ground state geometry obtained at the CAM-B3LYP level of theory. To be consistent with the (TD)DFT simulations, the 6–31G(d)[73] double-ζ basis set as well as the MWB28[74] relativistic core potential were applied.

For **Ru**, two RAS partitions were designed to reduce the number of CSFs and consequently the computational demand: A bpy-

centered (denoted RAS_{bpy}) and a thiazole-centered (denoted RAS_{thia}) AS; see Figure 7. Both RASs include the (10,7) of the ruthenium atom in the RAS2. These seven orbitals comprise two pairs of σ/σ* orbitals, reflecting the linear combinations of the $d_{x^2-y^2}$, d_{z^2} and lone-pairs of the ligands of suitable symmetry, as well as the d_{xy}, d_{xz} and d_{yz} orbitals of the ruthenium. Additionally, the RAS2 of RAS_{bpy} comprises the lowest two unoccupied π^*_{bpy} orbitals of the bpy ligands ($\pi^*_{bpy,1}$ and $\pi^*_{bpy,2}$) – these two orbitals are essential to describe low-lying $MLCT_{bpy}$ states. To improve the description of these two π^*_{bpy} orbitals, the four highest π_{bpy} orbitals of the bpy ligands ($\pi_{bpy,1}$-$\pi_{bpy,4}$) as well as the remaining two corresponding π^*_{bpy} orbitals ($\pi^*_{bpy,3}$ and $\pi^*_{bpy,4}$) were assigned to RAS1 and RAS3, respectively. The excitation level among the subspaces was restricted to singles and doubles. In consequence, a RAS_{bpy} (18,2,2;4,9,2) with 1 085 796 CSFs is obtained. The thiazole-centered RAS (RAS_{thia}) was constructed in a similar fashion. Besides the (10,7) of the ruthenium, the RAS2 comprises one pair of π_{thia}/π^*_{thia} orbitals ($\pi_{thia,6}$ and $\pi^*_{thia,1}$) to allow the description of $MLCT_{thia}$ and $ILCT_{thia}$ states. To refine the description of these two π orbitals, RAS1 and RAS3 hold the five highest occupied and five lowest unoccupied π_{thia}/π^*_{thia} orbitals of the thiazole ligand. This leads in consequence to a RAS_{thia} (22,2,2;5,9,5) with 3 876 090 CSFs. In synergy, these RASs allow an unbiased evaluation of $MLCT_{bpy}$, $MLCT_{thia}$, $ILCT_{thia}$ and metal-centered (MC) states. However, charge transfer phenomena among the thiazole and the bipyridine ligand sphere cannot be described. The π system of the terminal 4-methoxyphenyl moieties was not incorporated as the impact of these orbitals is marginal with respect to the low-lying excited states.[29]

Additionally, two simplified RAS_{bpy} and RAS_{thia} partitions were constructed, where the two pairs of σ/σ* orbitals were redistributed from RAS2 to RAS1 and RAS3, respectively. Thus, the bpy-centered RAS (18,2,2;6,5,4) and the thiazole-centered RAS (22,2,2;7,5,7) were obtained, while the number of CSFs was drastically reduced from 1085796 to 50449 (RAS_{bpy}) and from 3876090 to 55378 CSFs (RAS_{thia}), see Figure S1. Reducing the number of CSFs by two orders of magnitude hardly affects the description of $MLCT_{bpy}$, $MLCT_{thia}$ and $ILCT_{thia}$ states, however, MC states are merely described via singly and doubly excited configurations.

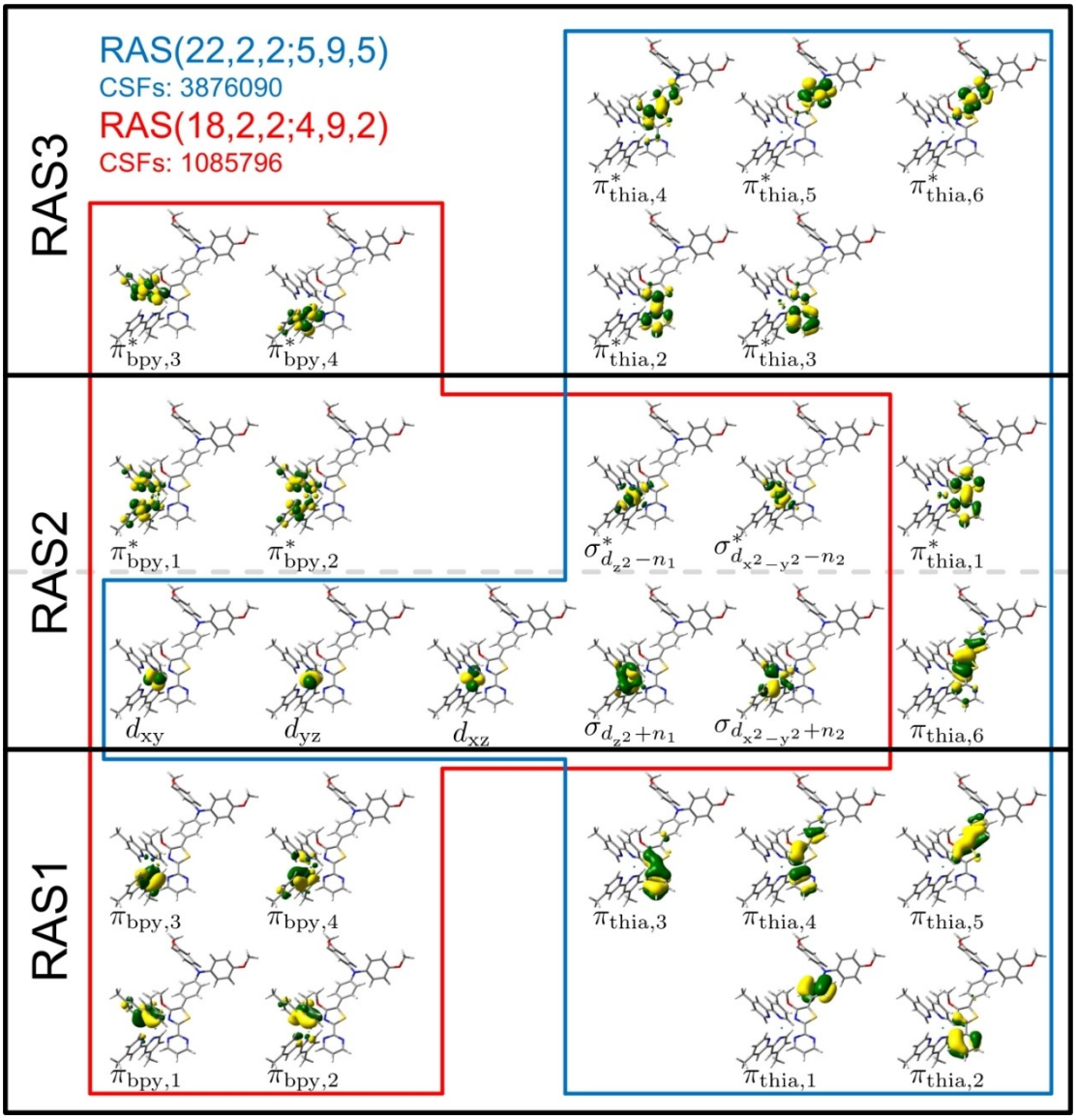

Figure 7. Molecular orbitals for the bpy-center RAS_{bpy} (18,2,2;4,9,2), highlighted in red, as well as the for the thiazole-center RAS_{thia} (22,2,2;5,9,5), highlighted in blue. The occupation of the molecular orbitals in the Hartree-Fock reference wavefunction is indicated (grey dashed line).

State-average (SA-)RASSCF calculations were carried out for the four RASs described above, i.e., comprising the first ten and the first eight roots for RAS_{bpy} and RAS_{thia}, respectively. The transition dipole moments were obtained at the SA-RASSCF level of theory using the CAS state interaction method.[100] Excited-state gradients at the Franck-Condon point were obtained exclusively for RAS_{bpy} (18,2,2;6,5,4), i.e., root seven of $MLCT_{bpy}$ character, and RAS_{thia} (22,2,2;7,5,7), i.e., roots four and five of $MLCT_{thia}$ and $ILCT_{thia}$ character, respectively.

The accuracy of the applied DFT and TDDFT as well as the multiconfigurational methods with respect to ground state equilibrium structures and Franck-Condon photophysical properties, such as excitation energies, transition dipole moments and excited-state gradients of prominent excited states, was evaluated based on **Ru**'s resonance Raman (RR) signal. The calculation of resonance Raman intensities – within the independent mode displacement harmonic oscillator model (IMDHOM) using the short-time approximation as well as the sum over states (SOS) formalism – was performed as reported in references[53,101] and references therein. The Raman response was simulated at excitation wavelengths of 514, 488 and 458 nm (2.41, 2.54 and 2.71 eV). Contributions from the bright singlet excitations involved in the absorption within the visible range, i.e., $MLCT_{bpy}$, $MLCT_{thia}$ and $ILCT_{thia}$ excitations, were considered, while a damping factor (Γ) of 0.372 eV reproduced the experimental absorption broadening. Within the SOS formalism, the $ILCT_{thia}$ excitation energy was set at 2.58 eV, while MLCT contributions ($MLCT_{thia}$ and $MLCT_{bpy}$) were set at an energy of 2.85 eV.

Acknowledgements

The authors are grateful for the support of the COST Action CM1202 Perspect-H_2O. Philipp Traber is acknowledged for providing the fractional occupation densities. All calculations have been performed at the Universitätsrechenzentrum of the Friedrich-Schiller University Jena. Open Access funding enabled and organized by Projekt DEAL.

Conflict of Interest

The authors declare no conflict of interest.

Data Availability Statement

Research data are not shared.

Keywords: light-harvesting · electron storage · resonance Raman spectroscopy · TDDFT · multiconfigurational calculations

[1] B. Zhang, L. Sun, *Chem. Soc. Rev.* **2019**, *48*, 2216–2264.
[2] N. Fajrina, M. Tahir, *Int. J. Hydrogen Energy* **2019**, *44*, 540–577.
[3] N. S. Lewis, D. G. Nocera, *Proc. Natl. Acad. Sci. USA* **2006**, *103*, 15729.
[4] K. S. Joya, Y. F. Joya, K. Ocakoglu, R. van de Krol, *Angew. Chem. Int. Ed.* **2013**, *52*, 10426–10437; *Angew. Chem.* **2013**, *125*, 10618–10630.
[5] N. Armaroli, V. Balzani, *Chem. Eur. J.* **2016**, *22*, 32–57.
[6] I. Roger, M. A. Shipman, M. D. Symes, *Nat. Chem. Rev.* **2017**, *1*, 0003.
[7] P. D. Frischmann, K. Mahata, F. Würthner, *Chem. Soc. Rev.* **2013**, *42*, 1847–1870.
[8] J. Nomrowski, O. S. Wenger, *J. Am. Chem. Soc.* **2018**, *140*, 5343–5346.
[9] T. Jiang, Y. Bai, P. Zhang, Q. Han, D. B. Mitzi, M. J. Therien, *Proc. Natl. Acad. Sci. USA* **2020**, *117*, 20430.
[10] F. M. Jradi, D. O'Neil, X. Kang, J. Wong, P. Szymanski, T. C. Parker, H. L. Anderson, M. A. El-Sayed, S. R. Marder, *Chem. Mater.* **2015**, *27*, 6305–6313.
[11] P. Dierks, A. Päpcke, O. S. Bokareva, B. Altenburger, T. Reuter, K. Heinze, O. Kühn, S. Lochbrunner, M. Bauer, *Inorg. Chem.* **2020**, *59*, 14746–14761.
[12] T. H. Bürgin, O. S. Wenger, *Energy Fuels* **2021**, *35*, 18848–18856.
[13] L. Hammarström, *Acc. Chem. Res.* **2015**, *48*, 840–850.
[14] J. M. Aslan, D. J. Boston, F. M. MacDonnell, *Chem. Eur. J.* **2015**, *21*, 17314–17323.
[15] J.-F. Lefebvre, J. Schindler, P. Traber, Y. Zhang, S. Kupfer, S. Gräfe, I. Baussanne, M. Demeunynck, J.-M. Mouesca, S. Gambarelli, V. Artero, B. Dietzek, M. Chavarot-Kerlidou, *Chem. Sci.* **2018**, *9*, 4152–4159.
[16] N. M. Randell, J. Rendon, M. Demeunynck, P.-A. Bayle, S. Gambarelli, V. Artero, J.-M. Mouesca, M. Chavarot-Kerlidou, *Chem. Eur. J.* **2019**, *25*, 13911–13920.
[17] J. Nomrowski, X. Guo, O. S. Wenger, *Chem. Eur. J.* **2018**, *24*, 14084–14087.
[18] M. Schulz, N. Hagmeyer, F. Wehmeyer, G. Lowe, M. Rosenkranz, B. Seidler, A. Popov, C. Streb, J. G. Vos, B. Dietzek, *J. Am. Chem. Soc.* **2020**, *142*, 15722–15728.
[19] K. Yatsuzuka, K. Yamauchi, K. Kawano, H. Ozawa, K. Sakai, *Sustain. Energy Fuels* **2021**, *5*, 740–749.
[20] S. Mendes Marinho, M.-H. Ha-Thi, V.-T. Pham, A. Quaranta, T. Pino, C. Lefumeux, T. Chamaillé, W. Leibl, A. Aukauloo, *Angew. Chem. Int. Ed.* **2017**, *56*, 15936–15940; *Angew. Chem.* **2017**, *129*, 16152–16156.
[21] R. Menzel, S. Kupfer, R. Mede, D. Weiß, H. Görls, L. González, R. Beckert, *Eur. J. Org. Chem.* **2012**, *2012*, 5231–5247.
[22] M. Kaufmann, C. Müller, A. A. Cullen, M. P. Brandon, B. Dietzek, M. T. Pryce, *Inorg. Chem.* **2021**, *60*, 760–773.
[23] E. Amouyal, A. Homsi, J.-C. Chambron, J.-P. Sauvage, *J. Chem. Soc. Dalton Trans.* **1990**, 1841–1845.
[24] C. Kuhnt, M. Karnahl, S. Tschierlei, K. Griebenow, M. Schmitt, B. Schäfer, S. Krieck, H. Görls, S. Rau, B. Dietzek, J. Popp, *Phys. Chem. Chem. Phys.* **2010**, *12*, 1357–1368.
[25] G. E. Shillito, C. B. Larsen, J. R. W. McLay, N. T. Lucas, K. C. Gordon, *Inorg. Chem.* **2016**, *55*, 11170–11184.
[26] Y. Zhang, P. Traber, L. Zedler, S. Kupfer, S. Gräfe, M. Schulz, W. Frey, M. Karnahl, B. Dietzek, *Phys. Chem. Chem. Phys.* **2018**, *20*, 24843–24857.
[27] D. Isakov, R. Giereth, D. Nauroozi, S. Tschierlei, S. Rau, *Inorg. Chem.* **2019**, *58*, 12646–12653.
[28] R. Menzel, D. Ogermann, S. Kupfer, D. Weiß, H. Görls, K. Kleinermanns, L. González, R. Beckert, *Dyes Pigm.* **2012**, *94*, 512–524.
[29] S. Kupfer, J. Guthmuller, L. González, *J. Chem. Theory Comput.* **2013**, *9*, 543–554.
[30] R. Menzel, S. Kupfer, R. Mede, H. Görls, L. González, R. Beckert, *Tetrahedron* **2013**, *69*, 1489–1498.
[31] S. H. Habenicht, M. Siegmann, S. Kupfer, J. Kübel, D. Weiß, D. Cherek, U. Möller, B. Dietzek, S. Gräfe, R. Beckert, *Methods Appl. Fluoresc.* **2015**, *3*, 025005.
[32] S. H. Habenicht, S. Kupfer, J. Nowotny, S. Schramm, D. Weiß, R. Beckert, H. Görls, *Dyes Pigm.* **2018**, *149*, 644–651.
[33] S. Kupfer, D. Kinzel, M. Siegmann, J. Philipp, B. Dietzek, S. Gräfe, *J. Phys. Chem. C* **2018**, *122*, 3273–3285.
[34] G. E. Shillito, T. B. J. Hall, D. Preston, P. Traber, L. Wu, K. E. A. Reynolds, R. Horvath, X. Z. Sun, N. T. Lucas, J. D. Crowley, M. W. George, S. Kupfer, K. C. Gordon, *J. Am. Chem. Soc.* **2018**, *140*, 4534–4542.
[35] L. González, D. Escudero, L. Serrano-Andrés, *ChemPhysChem* **2012**, *13*, 28–51.
[36] D. Escudero, W. Thiel, *J. Chem. Phys.* **2014**, *140*, 194105.
[37] S. Kupfer, J. Guthmuller, M. Wächtler, S. Losse, S. Rau, B. Dietzek, J. Popp, L. Gonzalez, *Phys. Chem. Chem. Phys.* **2011**, *13*, 15580–15588.
[38] C. Latouche, D. Skouteris, F. Palazzetti, V. Barone, *J. Chem. Theory Comput.* **2015**, *11*, 3281–3289.
[39] T. A. Niehaus, T. Hofbeck, H. Yersin, *RSC Adv.* **2015**, *5*, 63318–63329.
[40] T. Le Bahers, E. Brémond, I. Ciofini, C. Adamo, *Phys. Chem. Chem. Phys.* **2014**, *16*, 14435–14444.
[41] M. Fumanal, C. Daniel, *J. Comput. Chem.* **2016**, *37*, 2454–2466.

[42] J. J. Sutton, D. Preston, P. Traber, J. Steinmetzer, X. Wu, S. Kayal, X.-Z. Sun, J. D. Crowley, M. W. George, S. Kupfer, K. C. Gordon, *J. Am. Chem. Soc.* **2021**, *143*, 9082–9093.
[43] A. D. Becke, *J. Chem. Phys.* **1993**, *98*, 5648–5652.
[44] C. Lee, W. Yang, R. G. Parr, *Phys. Rev. B* **1988**, *37*, 785–789.
[45] G. García, C. Adamo, I. Ciofini, *Phys. Chem. Chem. Phys.* **2013**, *15*, 20210–20219.
[46] D. Jacquemin, A. Planchat, C. Adamo, B. Mennucci, *J. Chem. Theory Comput.* **2012**, *8*, 2359–2372.
[47] Z.-L. Cai, M. J. Crossley, J. R. Reimers, R. Kobayashi, R. D. Amos, *J. Phys. Chem. B* **2006**, *110*, 15624–15632.
[48] R. Li, J. Zheng, D. G. Truhlar, *Phys. Chem. Chem. Phys.* **2010**, *12*, 12697–12701.
[49] A. D. Laurent, D. Jacquemin, *Int. J. Quantum Chem.* **2013**, *113*, 2019–2039.
[50] J. Guthmuller, B. Champagne, *J. Chem. Phys.* **2007**, *127*, 164507.
[51] T. Yanai, D. Tew, N. Handy, *Chem. Phys. Lett.* **2004**, *393*, 51–57.
[52] M. Staniszewska, S. Kupfer, M. Łabuda, J. Guthmuller, *J. Chem. Theory Comput.* **2017**, *13*, 1263–1274.
[53] J. Guthmuller, *J. Chem. Phys.* **2016**, *144*, 064106.
[54] J. Guthmuller, *J. Chem. Phys.* **2018**, *148*, 124107.
[55] J. Guthmuller, *J. Chem. Phys.* **2021**, *155*, 084107.
[56] A. C. Bhasikuttan, M. Suzuki, S. Nakashima, T. Okada, *J. Am. Chem. Soc.* **2002**, *124*, 8398–8405.
[57] A. Cannizzo, F. van Mourik, W. Gawelda, G. Zgrablic, C. Bressler, M. Chergui, *Angew. Chem. Int. Ed.* **2006**, *45*, 3174–3176; *Angew. Chem.* **2006**, *118*, 3246–3248.
[58] E. A. Medlycott, G. S. Hanan, *Coord. Chem. Rev.* **2006**, *250*, 1763–1782.
[59] G. E. Shillito, D. Preston, P. Traber, J. Steinmetzer, C. J. McAdam, J. D. Crowley, P. Wagner, S. Kupfer, K. C. Gordon, *Inorg. Chem.* **2020**, *59*, 6736–6746.
[60] J. V. Caspar, T. J. Meyer, *J. Am. Chem. Soc.* **1983**, *105*, 5583–5590.
[61] J. Van Houten, R. J. Watts, *Inorg. Chem.* **1978**, *17*, 3381–3385.
[62] F. Barigelletti, A. Juris, V. Balzani, P. Belser, A. Von Zelewsky, *Inorg. Chem.* **1983**, *22*, 3335–3339.
[63] A. Juris, V. Balzani, F. Barigelletti, S. Campagna, P. Belser, A. von Zelewsky, *Coord. Chem. Rev.* **1988**, *84*, 85–277.
[64] A. T. Yeh, C. V. Shank, J. K. McCusker, *Science* **2000**, *289*, 935.
[65] J. P. Sauvage, J. P. Collin, J. C. Chambron, S. Guillerez, C. Coudret, V. Balzani, F. Barigelletti, L. De Cola, L. Flamigni, *Chem. Rev.* **1994**, *94*, 993–1019.
[66] A. Koch, D. Kinzel, F. Dröge, S. Gräfe, S. Kupfer, *J. Phys. Chem. C* **2017**, *121*, 16066–16078.
[67] Y. Liu, T. Harlang, S. E. Canton, P. Chábera, K. Suárez-Alcántara, A. Fleckhaus, D. A. Vithanage, E. Göransson, A. Corani, R. Lomoth, V. Sundström, K. Wärnmark, *Chem. Commun.* **2013**, *49*, 6412–6414.
[68] D. G. Brown, N. Sanguantrakun, B. Schulze, U. S. Schubert, C. P. Berlinguette, *J. Am. Chem. Soc.* **2012**, *134*, 12354–12357.
[69] T. Duchanois, T. Etienne, C. Cebrián, L. Liu, A. Monari, M. Beley, X. Assfeld, S. Haacke, P. C. Gros, *Eur. J. Inorg. Chem.* **2015**, *2015*, 2469–2477.
[70] S. Kupfer, *Phys. Chem. Chem. Phys.* **2016**, *18*, 13357–13367.
[71] A. K. Mengele, C. Müller, D. Nauroozi, S. Kupfer, B. Dietzek, S. Rau, *Inorg. Chem.* **2020**, *59*, 12097–12110.
[72] M. J. Frisch, G. W. Trucks, H. B. Schlegel, G. E. Scuseria, M. A. Robb, J. R. Cheeseman, G. Scalmani, V. Barone, B. Mennucci, G. A. Petersson, H. Nakatsuji, M. Caricato, X. Li, H. P. Hratchian, A. F. Izmaylov, J. Bloino, G. Zheng, J. L. Sonnenberg, M. Hada, M. Ehara, K. Toyota, R. Fukuda, J. Hasegawa, M. Ishida, T. Nakajima, Y. Honda, O. Kitao, H. Nakai, T. Vreven, J. A. Montgomery, J. E. Peralta, F. Ogliaro, M. Bearpark, J. J. Heyd, E. Brothers, K. N. Kudin, V. N. Staroverov, R. Kobayashi, J. Normand, K. Raghavachari, A. Rendell, J. C. Burant, S. S. Iyengar, J. Tomasi, M. Cossi, N. Rega, J. M. Millam, M. Klene, J. E. Knox, J. B. Cross, V. Bakken, C. Adamo, J. Jaramillo, R. Gomperts, R. E. Stratmann, O. Yazyev, A. J. Austin, R. Cammi, C. Pomelli, J. W. Ochterski, R. L. Martin, K. Morokuma, V. G. Zakrzewski, G. A. Voth, P. Salvador, J. J. Dannenberg, S. Dapprich, A. D. Daniels, Farkas, J. B. Foresman, J. V. Ortiz, J. Cioslowski, D. J. Fox, *Gaussian 09*, *Revision B.01*, Gaussian, Inc., Wallingford, CT, **2009**.
[73] P. C. Hariharan, J. A. Pople, *Theor. Chem. Acc.* **1973**, *28*, 213–222.
[74] D. Andrae, U. Häußermann, M. Dolg, H. Stoll, H. Preuß, *Theor. Chem. Acc.* **1990**, *77*, 123–141.
[75] J. P. Merrick, D. Moran, L. Radom, *J. Phys. Chem. A* **2007**, *111*, 11683–11700.
[76] R. Johnson, **2011**, DOI 10.18434/T47C7Z.
[77] M. J. G. Peach, M. J. Williamson, D. J. Tozer, *J. Chem. Theory Comput.* **2011**, *7*, 3578–3585.
[78] P. Kumar, D. Escudero, *Inorg. Chem.* **2021**, *60*, 17230–17240.
[79] B. Mennucci, C. Cappelli, C. A. Guido, R. Cammi, J. Tomasi, *J. Phys. Chem. A* **2009**, *113*, 3009.
[80] C. A. Bauer, A. Hansen, S. Grimme, *Chem. Eur. J.* **2017**, *23*, 6150–6164.
[81] S. Grimme, A. Hansen, *Angew. Chem. Int. Ed.* **2015**, *54*, 12308–12313; *Angew. Chem.* **2015**, *127*, 12483–12488.
[82] F. Neese, *WIREs Comput. Mol. Sci.* **2012**, *2*, 73–78.
[83] J. Tao, J. P. Perdew, V. N. Staroverov, G. E. Scuseria, *Phys. Rev. Lett.* **2003**, *91*, 146401.
[84] F. Weigend, R. Ahlrichs, *Phys. Chem. Chem. Phys.* **2005**, *7*, 3297–3305.
[85] F. Weigend, *Phys. Chem. Chem. Phys.* **2006**, *8*, 1057–1065.
[86] B. O. Roos, *In Ab Initio Methods in Quantum Chemistry II*, Wiley-VCH, Chinester, **1987**.
[87] T. Fleig, J. Olsen, C. M. Marian, *J. Chem. Phys.* **2001**, *114*, 4775–4790.
[88] D. Ma, G. Li Manni, L. Gagliardi, *J. Chem. Phys.* **2011**, *135*, 044128.
[89] K. D. Vogiatzis, G. Li Manni, S. J. Stoneburner, D. Ma, L. Gagliardi, *J. Chem. Theory Comput.* **2015**, *11*, 3010–3021.
[90] S. Ghosh, C. J. Cramer, D. G. Truhlar, L. Gagliardi, *Chem. Sci.* **2017**, *8*, 2741–2750.
[91] J. Ivanic, *J. Chem. Phys.* **2003**, *119*, 9364–9376.
[92] S. R. White, *Phys. Rev. Lett.* **1992**, *69*, 2863–2866.
[93] S. R. White, R. L. Martin, *J. Chem. Phys.* **1999**, *110*, 4127–4130.
[94] G. K.-L. Chan, S. Sharma, *Annu. Rev. Phys. Chem.* **2011**, *62*, 465–481.
[95] A. Baiardi, M. Reiher, *J. Chem. Phys.* **2020**, *152*, 040903.
[96] J. Olsen, B. O. Roos, P. Jørgensen, H. J. A. Jensen, *J. Chem. Phys.* **1988**, *89*, 2185.
[97] P. Å Malmqvist, A. Rendell, B. O. Roos, *J. Phys. Chem.* **1990**, *94*, 5477–5482.
[98] P. -Å Malmqvist, K. Pierloot, A. R. M. Shahi, C. J. Cramer, L. Gagliardi, *J. Chem. Phys.* **2008**, *128*, 204109.
[99] V. Sauri, L. Serrano-Andrés, A. R. M. Shahi, L. Gagliardi, S. Vancoillie, K. Pierloot, *J. Chem. Theory Comput.* **2011**, *7*, 153–168.
[100] P. -Å Malmqvist, B. O. Roos, *Chem. Phys. Lett.* **1989**, *155*, 189–194.
[101] M. Wächtler, J. Guthmuller, L. González, B. Dietzek, *Coord. Chem. Rev.* **2012**, *256*, 1479–1508.

Manuscript received: January 12, 2022
Revised manuscript received: February 10, 2022
Accepted manuscript online: February 11, 2022
Version of record online: March 3, 2022